

## Timing and Scintillation Studies of Pulsars in Globular Cluster M3 (NGC 5272) with FAST

BAODA LI<sup>1,2</sup>, LI-YUN ZHANG<sup>1,2</sup>, JUMEI YAO<sup>3,4,5</sup>, DEJIANG YIN<sup>1</sup>, RALPH P. EATOUGH<sup>6,7</sup>, MINGHUI LI,<sup>8</sup>  
YIFENG LI,<sup>9,10</sup> YUJIE LIAN<sup>11,12</sup>, YU PAN,<sup>13</sup> YINFENG DAI<sup>1</sup>, YAOWEI LI,<sup>1</sup> XINGNAN ZHANG,<sup>8</sup> TIANHAO SU,<sup>1</sup>  
YUXIAO WU,<sup>13</sup> TONG LIU,<sup>6</sup> KUO LIU<sup>14</sup>, LIN WANG<sup>15</sup>, LEI QIAN<sup>16,6,17,18</sup> AND ZHICHEN PAN<sup>16,6,17,18</sup><sup>1</sup> College of Physics, Guizhou University, Guiyang 550025, P.R. China<sup>2</sup> International Centre of Supernovae, Yunnan Key Laboratory, Kunming 650216, P.R. China<sup>3</sup> Xinjiang Astronomical Observatory, Chinese Academy of Sciences, 150, Science 1-Street, Urumqi, Xinjiang 830011, P. R. China<sup>4</sup> Key Laboratory of Radio Astronomy, Chinese Academy of Sciences, Urumqi, Xinjiang 830011, P. R. China<sup>5</sup> Xinjiang Key Laboratory of Radio Astrophysics, 150 Science1-Street, Urumqi, Xinjiang 830011, P. R. China<sup>6</sup> National Astronomical Observatories, Chinese Academy of Sciences, 20A Datun Road, Chaoyang District, Beijing 100101, P.R. China<sup>7</sup> Max-Planck-Institut für Radioastronomie, Auf dem Hügel 69, D-53121, Bonn, Germany<sup>8</sup> State Key Laboratory of Public Big Data, Guizhou University, Guiyang 550025, P.R. China<sup>9</sup> National Time Service Center, Chinese Academy of Sciences, Xi'an, 710600, P.R. China<sup>10</sup> Key Laboratory of Time Reference and Applications, Chinese Academy of Sciences, Xi'an, 710600, P.R. China<sup>11</sup> Institute for Frontiers in Astronomy and Astrophysics, Beijing Normal University, Beijing 102206, P.R. China<sup>12</sup> Department of Astronomy, Beijing Normal University, Beijing 100875, P.R. China<sup>13</sup> Chongqing University of Posts and Telecommunications, Chongqing, 40000, P.R. China<sup>14</sup> Shanghai Astronomical Observatory, Chinese Academy of Sciences, Shanghai, 200030, P.R. China<sup>15</sup> Kavli Institute for Astronomy and Astrophysics, Peking University, Beijing 100871, P.R. China<sup>16</sup> Guizhou Radio Astronomical Observatory, Guizhou University Guiyang 550025, P.R. China<sup>17</sup> CAS Key Laboratory of FAST, National Astronomical Observatories, Chinese Academy of Sciences, Beijing 100101, P.R. China<sup>18</sup> College of Astronomy and Space Sciences, University of Chinese Academy of Sciences, Beijing 100049, P.R. China

## ABSTRACT

We present the phase-connected timing solutions of all the five pulsars in globular cluster (GC) M3 (NGC 5272), namely PSRs M3A to F (PSRs J1342+2822A to F), with the exception of PSR M3C, from FAST archival data. In these timing solutions, those of PSRs M3E, and F are obtained for the first time. We find that PSRs M3E and F have low mass companions, and are in circular orbits with periods of 7.1 and 3.0 days, respectively. For PSR M3C, we have not detected it in all the 41 observations. We found no X-ray counterparts for these pulsars in archival Chandra images in the band of 0.2–20 keV. We noticed that the pulsars in M3 seem to be native. From the Auto-Correlation Function (ACF) analysis of the M3A's and M3B's dynamic spectra, the scintillation timescale ranges from  $7.0 \pm 0.3$  min to  $60.0 \pm 0.6$  min, and the scintillation bandwidth ranges from  $4.6 \pm 0.2$  MHz to  $57.1 \pm 1.1$  MHz. The measured scintillation bandwidths from the dynamic spectra indicate strong scintillation, and the scattering medium is anisotropic. From the secondary spectra, we captured a scintillation arc only for PSR M3B with a curvature of  $649 \pm 23 \text{ m}^{-1} \text{ mHz}^{-2}$ .

**Keywords:** Pulsar timing; Millisecond pulsars; Binary pulsars; Interstellar scintillation; Globular star clusters;

Corresponding author: Li-yun Zhang, Jumei Yao, Lei Qian, Zhichen Pan

liy\_zhang@hotmail.com

yaojumei@xao.ac.cn

lqian@nao.cas.cn

panzc@bao.ac.cn

## 1. INTRODUCTION

Globular clusters (GCs) with very high stellar number density have been proven to be factories of millisecond pulsars (MSPs) (Freire et al. 2017). The GC M3 (NGC 5272) is located 10.2 kpc away (Harris 1996). At present, six pulsars have been found in this cluster, namely PSRs M3A to F, or PSRs J1342+2822A to F. All of them are MSP binaries with dispersion measures (DMs) around  $26.4 \text{ pc cm}^{-3}$ . PSRs M3A to D were found by Arecibo and Green Bank Telescope (GBT) (Ransom et al. 2005; Hessels et al. 2007), while PSRs M3E and F (Pan et al. 2021) were found by the Five-hundred-meter Aperture Spherical radio Telescope (FAST, Nan et al. 2011).

PSR M3A is a black widow with a minimum companion mass of  $0.01 M_{\odot}$  and an orbital period of 0.14 days (Pan et al. 2021). PSR M3B has a minimum companion mass of  $0.21 M_{\odot}$  and an orbital period of 34.0 hours (Hessels et al. 2007). PSR M3C was detected only once by GBT (Ransom et al. 2005), and is still to be confirmed at other telescopes. PSR M3D has a companion with a minimum mass of  $0.21 M_{\odot}$  and an orbital period of 129 days. Such an orbit indicates that PSR M3D probably experienced abnormal evolution (Hessels et al. 2007).

Due to scintillation, the detection rates of pulsars in M3 from previous studies are quite low. For example, in 78 observations with Arecibo and GBT, PSRs M3A to D only appeared three times, 16 times, once (at GBT), and 12 times, respectively (Hessels et al. 2007). Only the timing solutions of PSRs M3B and D have been obtained.

When a pulsar radio signal propagates through the turbulent ionized interstellar medium (ISM), the relative motion between the pulsar, the ISM and the Earth lead to scintillation, which changes the pulsar intensity (Rickett 1990). There are two main types of pulsar scintillation, namely refractive interstellar scintillation (RISS) and diffractive interstellar scintillation (DISS). RISS from the large-scale inhomogeneity of the ISM leads to a long-term (e.g., days to months) fluctuation of pulsar flux densities (Rickett et al. 1984; Blandford et al. 1986). DISS from the small-scale inhomogeneities in the ISM leads to short time-scale (e.g., minutes to hours) variations of pulsar flux densities (Rickett 1969).

For DISS, scintillation bandwidth  $\Delta\nu_d$  and scintillation timescale  $\Delta\tau_d$  can be obtained from the Auto-Correlation Function (ACF) analysis of a pulsar dynamic spectrum, which is a map of pulsar intensity as a function of observing frequency and time. The  $\Delta\tau_d$  is the half width of ACF at  $1/e$  along the time axis, and  $\Delta\nu_d$  is the half width at the half maximum along the frequency axis (Cordes et al. 1986). The scintillation bandwidth can be used to determine the scintillation strength (Rickett 1990). Studies on pulsar scintillation can help us to reveal properties of the ISM, for example, its anisotropic or isotropic nature (Wang et al. 2005). The secondary spectrum is the squared modulus of the two dimensional Fourier transform of a dynamic spectrum. In some situations, we can detect so-called scintillation arcs (one or many) in the secondary spectrum (Stinebring et al. 2001). For pulsars with distance and proper motion measurements, it is possible to obtain the density, scale and location of screen-like ISM structures through the detection of the scintillation arcs or arclets in the secondary spectrum (Hill et al. 2005; Yao et al. 2020). For pulsars in binary systems, the scintillation timescale and the arc curvature are modulated by orbital motion, and their measurements may enable us to constrain both the binary orbital inclination and the distance of the scattering screen (Reardon et al. 2019).

With FAST, the detection rates of pulsars in M3 are more than twice, those seen in previous studies. This increased rate provides a better opportunity to study the properties of pulsars in M3 though both pulsar timing and observations of scintillation along the line of sight to this GC. In this paper, we update the ephemerides of PSRs M3A, B, and D, and report the timing solutions of PSRs M3E and F and an analysis of the scintillation properties of PSRs M3A and B in M3. In Section 2 the data reduction methods used are described. Section 3 presents the results and discusses the detection rates and timing solutions; encounter rates and eccentricities; cluster acceleration; and scintillation properties. In Section 4, we give a short summary.

## 2. DATA REDUCTION

We analyzed the FAST archival data of all the 41 observations. All these data were recorded with the 19-beam L-band receiver covering a frequency range of 1.0 to 1.5 GHz (Jiang et al. 2020). Because the core radius of M3 ( $0.37'$ ) fits within the half-power beamwidth of a single receiver ( $3'$ ), only data from the central beam was used in our study. The signals were 8-bit sampled with two or four polarization products and recorded in PSRFITS format (Hotan et al. 2004). The number of frequency channels used is 4096 (corresponding to a 0.122 MHz channel width), and the sampling time is  $49.152 \mu\text{s}$ . All 41 observations are pointed toward the center of M3 at right ascension (RA) (J2000) 13:42:12.00 and declination (DEC) (J2000) +28:22:38.2, with observation times range from 20 minutes to 5 hours on dates from MJD 58831 to 59767.

### 2.1. Data Reduction for Timing

According to the previous studies, PSRs M3B (orbital period  $\sim 1.4$  day) and D ( $\sim 129$  day) have timing solutions (Hessels et al. 2007), PSR M3A was proved to be a black widow ( $\sim 0.14$  day) based on only two observations (Pan et al. 2021). The published ephemerides of PSRs M3B and D have not been updated for almost 20 years, and cover MJDs 52763 to 53542 and 52768 to 53476, respectively (Hessels et al. 2007). PSR M3C, if it is a real pulsar, was only seen once by GBT (Ransom et al. 2005) but is believed to be in a binary system (Hessels et al. 2007). In order to re-detect all the pulsars in M3, we folded the data with the timing solutions, and also performed blind searches to account for any significant offsets accrued in the spin frequency over the intervening years, or from unknown orbital modulation. The software used for searching and folding was PRESTO<sup>1</sup> (Ransom 2001, 2011) and TEMPO<sup>2</sup> was used to either create or update timing solutions. The routine RFIFIND from PRESTO was used for generating radio frequency interference (RFI) masks. The length of data for finding radio frequency domain RFI (`-time` option) was 12.9s. The routine PREPDATA was used to dedisperse the data. Considering the possible range of DMs in a given GC (Yin et al. 2023), the range used for M3 was 24.5 to 28.5 pc cm<sup>-3</sup>. In order to catch any possible faint signals, a DM step of 0.01 pc cm<sup>-3</sup> was used for dedispersion. Then, a Fast Fourier Transform was applied to the dedispersed time series to obtain fluctuation spectra. The routine ACCELSEARCH was used to search for possible periodic signals in the spectra where the largest range in acceleration (defined by the ACCELSEARCH parameter `-zmax`) was set to be 1200, where `-zmax` represents the number of Fourier bins that a signal can drift during an individual observation. All periodic signals with a clearly defined DM were folded using the routine PREPFOLD to produce so-called candidate plots that were visually checked. As a result, PSRs M3A, B, D, E, and F were detected on multiple occasions (24, 37, 32, 21 and 33 times, respectively) enough to construct updated timing solutions.

The routine GET\_TOAS.PY from PRESTO was used to obtain the times of arrivals (ToAs). Standard reference profile templates for correlation (to measure ToAs) were obtained by fitting the pulse profiles from the detection with the highest signal-to-noise ratios (SNRs) with the PRESTO routine PYGAUSSFIT.PY. According to the SNR of the pulsar signal, the number of ToAs obtained from each observation ranged from 4 to 16. For PSRs M3E and F, we used the FITORB.PY routine<sup>3</sup> to fit for the initial orbital parameters. With the initial parameter files from either the PSRCAT (PSRs M3A, B, and D) or orbit fitting (PSRs M3E and F), the phase-connected timing solutions for PSRs M3A, B, D, E, and F were obtained. Figure 1 shows integrated pulse profiles and timing residuals from the FAST observations and Table 1 presents the timing solutions for the five M3 pulsars.

### 2.2. Data Reduction for Scintillation

PREPFOLD from PRESTO was used to create the standard period folded archive files that are the basis for scintillation studies. Each archive had a sub-integration time and frequency channel resolution of 60 s and 0.98 MHz, respectively. Then, PAZI, PAM, and PSRFLUX from PSRCHIVE were used to analyze the data (van Straten et al. 2012). Then, PAZI was used to manually remove RFI. Second, the routine PAM was used to sum the polarization channels to total intensity. Third, PSRFLUX was used to generate the dynamic spectrum from the archive files.

The scintillation bandwidth and scintillation timescale can be obtained from the ACF analysis of the dynamic spectrum. The ACF  $C(\Delta\nu, \Delta\tau)$ , where  $\Delta\nu$  and  $\Delta\tau$  are the frequency and time lag, respectively, is defined by the formula (Zhang et al. 2023 and references therein):

$$C(\Delta\nu, \Delta\tau) = \sum_{\nu} \sum_t \Delta D(\nu, t) \Delta D(\nu + \Delta\nu, t + \Delta\tau), \quad (1)$$

where  $D(\nu, t)$  is the pulsar intensity as a function of frequency,  $\nu$  and time,  $t$ . Here  $\Delta D(\nu, t) = D(\nu, t) - \bar{D}$  (where “ $\bar{\phantom{x}}$ ” denotes averaging). The normalized ACF is  $N(\Delta\nu, \Delta\tau) = C(\Delta\nu, \Delta\tau)/C(0, 0)$ . Following Reardon (2020), we use their Scintools package<sup>4</sup> to calculate the ACF in this work.

The secondary spectrum is obtained from the two dimensional Fourier transform of the dynamic spectrum. We got the secondary spectrum with the equation (Reardon 2020)

$$P(f_t, f_\lambda) = 10 \log_{10}(|\tilde{D}(t, \lambda)|^2), \quad (2)$$

<sup>1</sup> <https://github.com/scottransom/presto>

<sup>2</sup> <http://pulsar.princeton.edu/tempo>

<sup>3</sup> <https://github.com/scottransom/presto/blob/master/bin/fitorb.py>

<sup>4</sup> <https://github.com/danielreardon/scintools>

**Table 1. Timing solutions of PSRs M3A, B, D and PSRs M3E, F. The Solar System Ephemeris we used is DE438, Time Units is TDB, and we did not use the clock correction file.**

Pulsar	M3A	M3B	M3D	M3E	M3F
Right Ascension, $\alpha$ (J2000) .....	13:42:13.79168(8)	13:42:11.08686(2)	13:42:11.35220(9)	13:42:12.3908(4)	13:42:12.37908(6)
Declination, $\delta$ (J2000) .....	28:23:01.966(1)	28:22:40.0844(2)	28:22:30.160(1)	28:23:16.131(6)	28:22:37.270(1)
Spin Frequency, $f$ ( $\text{s}^{-1}$ ) .....	392.96772541864(1)	418.5114725920(2)	183.7230520500(1)	182.7196423300(2)	227.07633075643(2)
1st Spin Frequency derivative, $\dot{f}$ ( $\text{Hz s}^{-2}$ ) .....	$1.5704(8)\times 10^{-15}$	$-3.2743(3)\times 10^{-15}$	$-9.47(2)\times 10^{-16}$	$3.5(7)\times 10^{-17}$	$-1.610(1)\times 10^{-15}$
Reference Epoch (MJD) .....	59194.14	52770.00	52770.00	59203.93	59291.67
Start of Timing Data (MJD) .....	58830.98	58830.98	59149.08	58831.00	58830.99
End of Timing Data (MJD) .....	59767.57	59767.58	59767.52	59767.57	59767.58
Dispersion Measure, DM ( $\text{pc cm}^{-3}$ ) .....	26.4278(8)	26.1510(4)	26.3677(3)	26.521(7)	26.436(2)
Number of TOAs .....	388	585	239	71	254
Residuals RMS ( $\mu\text{s}$ ) .....	20.33	7.11	12.05	36.27	19.66
Binary Model .....	ELL1	ELL1	BT	ELL1	ELL1
Projected Semi-major Axis, $x_p$ (lt-s) .....	0.0256212(7)	1.8756549(3)	38.521421(2)	5.33923(1)	2.225893(4)
Orbital Eccentricity, $e$ .....	–	–	$7.47556(1)\times 10^{-2}$	–	–
Longitude of Periastron, $\omega$ (deg) .....	–	–	206.18223(2)	–	–
Epoch of passage at Periastron, $T_0$ (MJD) .....	–	–	52655.44931(5)	–	–
First Laplace-Lagrange parameter, $\eta$ .....	$3(5)\times 10^{-5}$	$4.0(3)\times 10^{-6}$	–	$3.04(5)\times 10^{-4}$	$3(4)\times 10^{-6}$
Second Laplace-Lagrange parameter, $\kappa$ .....	$-6(5)\times 10^{-5}$	$6(4)\times 10^{-7}$	–	$-5.5(4)\times 10^{-5}$	$4(5)\times 10^{-6}$
Epoch of passage at Ascending Node, $T_{\text{asc}}$ (MJD)	58831.220370(2)	52485.967961(2)	–	59195.297476(4)	59231.715533(1)
Orbital Period, $P_b$ (days) .....	0.1358561044(3)	1.4173522991(3)	128.7454866(5)	7.0968527(1)	2.991987692(4)
Offset from GC center in $\alpha$ , $\theta_\alpha$ .....	-0.4775	-0.1173	+0.0589	-0.1695	+0.1670
Offset from GC center in $\delta$ , $\theta_\delta$ .....	+0.3961	+0.0314	-0.1340	+0.6322	-0.0155
Total offset from GC center, $\theta_\perp$ (arcmin) .....	0.6204	0.1214	0.1464	0.6545	0.1677
Total offset from GC center, $\theta_\perp$ (core radii) .....	1.6768	0.3281	0.3956	1.7690	0.4532
Projected distance from GC center, $r_\perp$ (pc) .....	1.8408	0.3602	0.4343	1.9420	0.4975

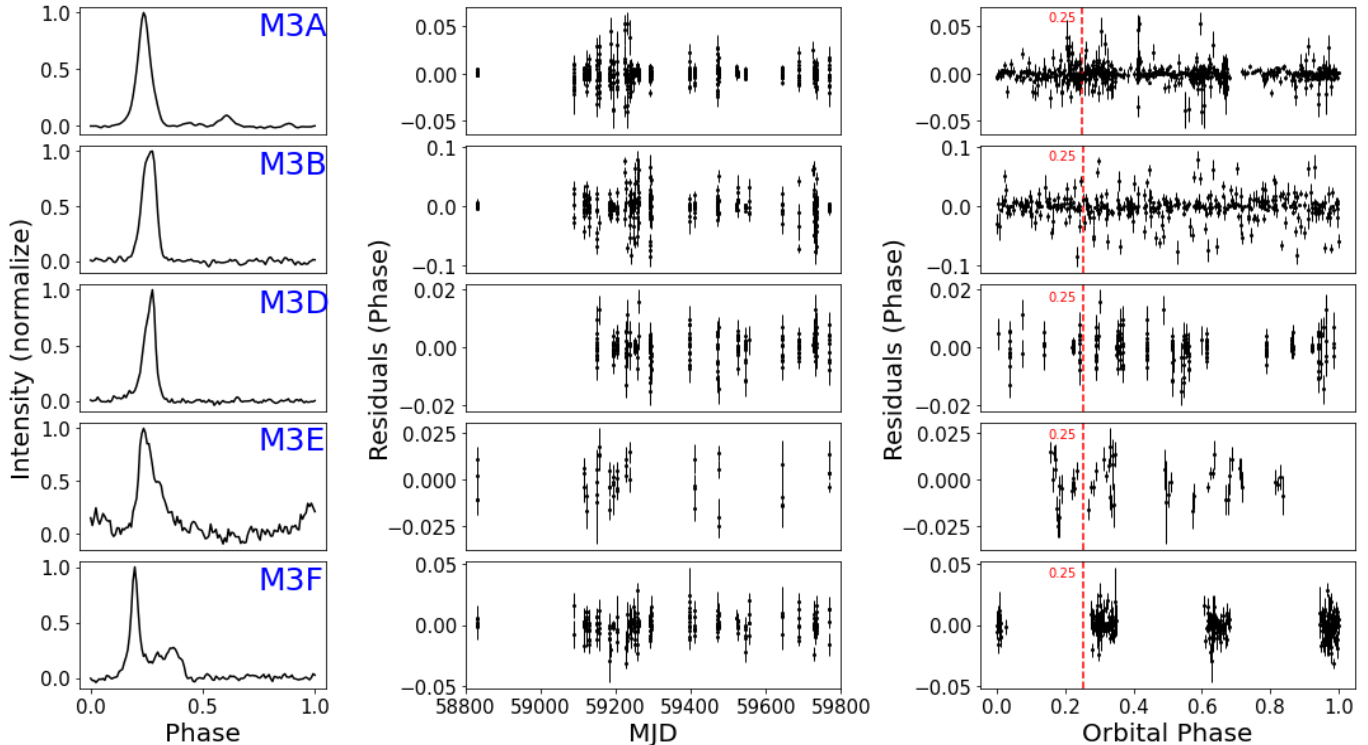


**Figure 1.** Profiles of PSRs M3A, B, D, E, and F (left panels), timing residuals for PSRs M3A, B, D, E, and F as a function of MJD (middle panels), and orbital phase (right panels). In the right panels, the orbital phase of 0.25 is marked by the red dashed lines, which is superior conjunction for pulsars in circular orbits. Except for PSR M3F, which was not covered, none of them showed eclipsing phenomena.

where the  $\tilde{\cdot}$  symbol denotes the two-dimensional Fourier transform, and  $f_t$  and  $f_\lambda$  are the conjugate time and the conjugate wavelength, respectively. The transformed data are squared, shifted and cropped for the study.

### 3. RESULTS & DISCUSSION

#### 3.1. Detection Rates and Timing Solutions

The known pulsars in M3 are all in binary systems and all show scintillation. This can be seen from the fluctuations in the detected folded SNR given in Table 2. The previous searches for pulsars in M3 were carried out with Arecibo (Hessels et al. 2007) where observations covered a frequency range of 1.1 to 1.6 GHz. The corresponding detection rates of PSRs M3A to D were 4%, 21%, once, and 15%, respectively. With FAST, the detection rates of pulsars in M3 are greatly improved, except for PSR M3C. In the 41 FAST archival data, PSRs M3A to F were detected for 24 (58%), 37 (90%), 0, 32 (78%), 21 (51%), and 33 (80%) times, respectively (see Table 3).

In order to catch PSR M3C, we searched for it with the whole length of the data and some 5, 30, and 100 minutes segments. In all these searches, the value of the ACCELSEARCH option which determines the range of accelerations searched ( $-zmax$ ) was set to 1200. Then, we searched for any possible signals which have periods around 2.166 ms (PSR M3C). Unfortunately, no pulsar-like signals were detected. Therefore, we postulate that PSR M3C was discovered undergoing extreme scintillation – like PSR M30B in Ransom et al. (2004) – which has recently been detected again with MeerKat only for the second time in Balakrishnan et al. (2023), or the detection candidate was possibly due to noise fluctuation.

With the FAST data, we derived the phase-connected timing solutions of PSRs M3A, B, D, E, and F. The results of PSRs M3A, B, and D were consistent with the previous studies: PSR M3A (Pan et al. 2021) and PSRs M3B and D (Hessels et al. 2007), with slight differences in positions, spin frequencies, and spin frequency derivatives. For example, the DEC,  $\delta$  of PSR M3B is  $+28:22:40.141(2)$  in Hessels et al. (2007), and the result given here is  $+28:22:40.0844(2)$ ; a small difference of  $0.06''$ . The difference in  $\delta$  is a slight difference may be caused by the

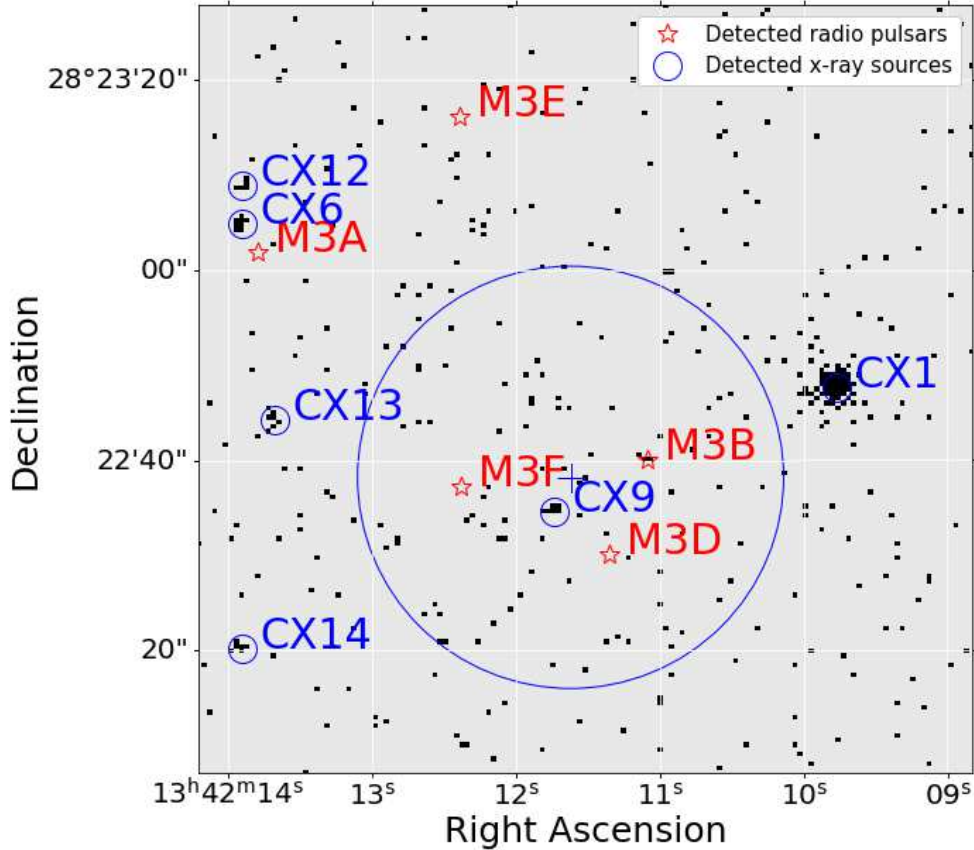


**Figure 2.** The radio pulsars and the X-ray sources of M3 in the Chandra image. PSRs M3A, B, D, E, and F are presented by the red stars. The X-ray sources are marked by the small blue circles. The center of M3 (J2000, RA 13:42:11.62 DEC +28:22:38.2) is shown as a blue cross. The large blue circle represents the core radius of 0.37 arcminutes. The energy range for the background X-ray image is from 0.2 to 20 keV.

longer baseline and more timing data (16 detections covering 779 days in [Hessels et al. \(2007\)](#), 37 detections covering 937 days in this work).

PSR M3A is a black widow in a 0.14-day orbit. The minimum companion mass is around  $0.01 M_{\odot}$ . No eclipsing was observed. The timing solution of PSR M3D was greatly improved with errors in RA and DEC being reduced by factors of 1000 and 10,000 times, respectively.

PSRs M3E and F are two pulsars recently discovered by FAST ([Pan et al. 2021](#)). With a detection rate of 50%, PSR M3E has a period of 5.473 ms and a DM value of  $26.5 \text{ pc cm}^{-3}$ . It is in an orbit of 7.1 days with a minimum companion mass of  $0.2 M_{\odot}$ . The eccentricity of its orbit is small but detectable, being  $\sim 4.5 \times 10^{-4}$ . Showing faint signals, PSR M3F has a high detection rate of 80%, only 10% lower than that of PSR M3B. Its period and DM are 4.404 ms and  $26.4 \text{ pc cm}^{-3}$ , respectively. It is in an orbit of 3 days with a minimum companion mass of  $0.17 M_{\odot}$ . It seems that all the 33 detections of PSR M3F only appeared on the orbital phases of approximately 0.00, 0.33, and 0.67. The orbital period of PSR M3F is almost exactly 3 sidereal days in duration. And since FAST is (mostly) a transit telescope, when we observe on a random day over a relatively short timespan (a year or two), we sample only 1 of 3 different orbital phases. It will take a long time for the very small deviation of  $P_b/3$  from a sidereal day to allow full-sampling of the full orbit.

### 3.2. X-ray source associations

The core radius of M3 is  $0.37'$ . The PSRs M3A and E are out of the core region while PSRs M3B, D, and F are in the core region. Generally, rotation-powered MSPs are weak X-ray sources ([Bogdanov et al. 2021](#)). Fig. 2 shows the position of M3 pulsars overlaid on an X-ray image from archival Chandra data. Six bright X-ray sources ([Zhao et al.](#)

**Table 2.** The SNRs for all observations of M3 pulsars (except for PSR M3C) made at FAST. For each pulsar, the lowest and the highest SNRs are marked with wavy line and underline, respectively.

Data YYYYMMDD	MJD	Observation Length (s)	M3A (SNR)	M3B (SNR)	M3D (SNR)	M3E (SNR)	M3F (SNR)
20191214	58831	16200	28.2	67.3		4.0	7.8
20200828	59089	1800		10.4			
20200923	59115	7200	9.8	41.4		5.0	15.8
20200929	59121	7200		10.5		<u>2.9</u>	7.0
20201008	59130	7200	6.0	16.4	5.4		6.3
20201027	59149	14400		<u>4.9</u>	26.4	3.8	8.7
20201102	59155	18000		10.3	4.6	4.0	
20201130	59183	18000	13.7	18.0	<u>3.5</u>	5.9	5.5
20201205	59188	5880	10.2				
20201211	59194	18000	34.2	16.7	30.0	6.3	23.8
20201221	59204	11115	8.4	7.5	22.7	5.6	
20210112	59226	18015		29.8	11.9	7.6	
20210117	59231	2715			7.7		
20210125	59239	18015	4.7	17.7	8.6	4.8	<u>24.1</u>
20210126	59240	18015	18.0	50.7	5.3	3.6	<u>4.8</u>
20210204	59249	18015		33.3	7.6		10.2
20210205	59250	14160	4.2	69.2	41.6	4.2	10.2
20210214	59259	14400		22.7	8.7		
20210215	59260	18015	<u>4.0</u>	18.0	4.0		11.9
20210318	59291	18015	6.6	16.3	6.6		10.0
20210319	59292	18015		37.2	10.0		17.0
20210320	59293	18015	6.2	51.1	27.0	3.6	6.2
20210321	59294	19184		63.4	7.9	5.1	10.6
20210701	59396	18000	11.0	14.8	10.0		8.4
20210702	59397	18320	4.7	69.1	8.0		6.8
20210714	59409	16377	7.1	9.7		6.0	8.1
20210914	59471	14400	4.5	10.5	16.6	3.6	9.6
20210915	59472	14400	13.4		6.2		23.3
20210916	59473	14400		36.6	9.0	5.6	18.7
20211105	59523	14400	22.2	33.0			
20211106	59524	11400		<u>70.5</u>	24.4		9.1
20211127	59545	13800	32.8	32.6	15.4	5.4	5.7
20211208	59556	14400					14.6
20220307	59645	11115	5.8	30.8	13.2	5.1	4.1
20220418	59687	5040		22.9	21.9	4.0	7.1
20220527	59726	7980		23.0	<u>45.4</u>		
20220530	59729	14715	11.9	35.1	5.0		16.0
20220601	59731	7740		40.5	8.4		13.2
20220604	59734	4380		40.8	6.8		10.6
20220606	59736	5880	8.9	14.1			9.9
20220707	59767	16980	<u>46.2</u>	10.2	13.9	<u>7.8</u>	6.0

**Table 3.** Comparison of M3 pulsar detection rates (given as a percentage of observations performed) at three telescopes. For brevity we have removed the “PSR” notation from each pulsar name and “-” indicates either un-published or non-applicable detection rates.

	M3A	M3B	M3C	M3D	M3E	M3F
FAST	58%	90%	-	78%	51%	80%
Arecibo	4%	21%	-	13%	-	-
GBT	-	-	once	-	-	-

2019) near the GC center were detected by Chandra (see blue circles in Fig. 2). The known pulsars are represented by the red stars. No X-ray counterparts were identified for any pulsar in M3.

### 3.3. The Single-Binary Encounter Rate and Eccentricities

The percentage of binary pulsars in a GC is related to the single-binary encounter rate (Lian et al. 2023),

$$\gamma \propto \frac{\rho_c}{v}, \quad (3)$$

where  $\rho_c$  is the GC central density and  $v$  is the velocity dispersion (Lian et al. 2023). When  $\gamma$  is normalized to the value for M4, being  $\gamma_{M4}$  as in Verbunt & Freire (2014). The  $\gamma_{M4}$  of M3 is 0.62. The pulsars in M3 are all in binary systems, it is similar to other GCs with low  $\gamma_{M4}$ , e.g. M13,  $\gamma_{M4} = 0.52$ , four binaries and two isolated (Wang et al. 2020). In GCs with small  $\gamma_{M4}$ , X-ray binaries are expected to evolve without much interference, forming binary MSPs similar to those in the Galactic disk.

In M3, the eccentricity of pulsars is close to 0, except for PSR M3D (0.075). It is in a very long orbit of about 129 days. Its orbital period is much longer than the typical orbital period (1 day) of GC MSPs. Only 16 among 177 GC binary pulsars<sup>5</sup> are with orbital periods larger than 10 days. They are believed to be formed through an exchange interaction between an isolated neutron stars and primordial cluster binaries, and pulsars with orbital periods greater than 100 days tend to reside in low-density clusters with the central density  $\rho_c$  less than  $4 \log_{10} L_{\odot} \text{ pc}^{-3}$  (Hut et al. 1992; Sigurdsson & Phinney 1993). As M3 has a central density  $\rho_c = 3.72 \log_{10} L_{\odot} \text{ pc}^{-3}$ , PSR M3D follows this trend. Its eccentricity is likely the result of passing-by encounters with other binaries. The time scale needed to produce the eccentricity of PSR M3D can be estimated as in Rasio & Heggie (1995); Lian et al. (2023):

$$t_e \simeq 4 \times 10^{11} \text{ yr} \left( \frac{n}{10^4 \text{ pc}^{-3}} \right)^{-1} \left( \frac{v}{10 \text{ km s}^{-1}} \right) \times \left( \frac{P_b}{\text{days}} \right)^{-2/3} e^{2/5}, \quad (4)$$

where  $n$  is the number density of stars ( $n \propto \rho_c$ ,  $\rho_c$  is the central density of GC, which is  $3.72 \times 10^3 L_{\odot} \text{ pc}^{-3}$  for M3 (Harris 1996)),  $v$  is the one-dimensional core velocity dispersion, which is  $7.8 \text{ km s}^{-1}$  for M3<sup>6</sup> (Libralato et al. 2022),  $P_b$  is the orbital period, and  $e$  is the eccentricity. Following Lian et al. (2023),  $n$  is roughly estimated as  $8.9 \times 10^3 \text{ pc}^{-3}$  for M3. The estimated  $t_e$  is  $\sim 4.8 \text{ Gyr}$ , and the characteristic age of M3 is  $8.7 \text{ Gyr}$  (Hamrick et al. 2021). This shows that PSR M3D has had enough time to accumulate the eccentricity caused by disturbance.

### 3.4. Acceleration Caused by Cluster Gravity

From timing results, we noticed that the spin period derivatives of PSRs M3A and E are negative. Usually, the intrinsic spin period derivative of a pulsar should be positive. Like other pulsars in GCs, the negative spin period derivative is expected to be caused by the contribution of the gravitational potential of the GC (Phinney 1993). In general, the observed spin period derivative can be described by

$$c \left( \frac{\dot{P}}{P} \right)_{\text{obs}} - c \left( \frac{\dot{P}}{P} \right)_{\text{int}} = \frac{V_{\perp}^2}{d} + a_g + a_{\ell, GC}, \quad (5)$$

where  $P$  is the pulsar spin period,  $\dot{P}$  is the spin period derivative,  $V_{\perp}$  is the transverse velocity of the system,  $d$  is the distance to the pulsar,  $a_g$  is the acceleration due to the Galactic potential,  $a_{\ell, GC}$  the line-of-sight acceleration due to

<sup>5</sup> <https://www3.mpifr-bonn.mpg.de/staff/pfreire/GCpsr.html> (accessed on 15 January 2024)

<sup>6</sup> <https://people.smp.uq.edu.au/HolgerBaumgardt/globular/orbits.html>

the GC and  $c$  is the speed of light. The term  $\frac{V_d^2}{d}$  is the contribution of the Shklovskii effect (Shklovskii 1970). The proper motion and the distance of pulsars in M3 have not been determined, however, they should be similar to that of M3 itself. The proper motion of M3 in RA  $\alpha$  and DEC  $\delta$  is  $-0.153 \pm 0.007$  mas yr $^{-1}$  and  $-2.679 \pm 0.007$  mas yr $^{-1}$ , respectively. The distance,  $d$ , is  $\sim 10.2$  kpc (Vasiliev & Baumgardt 2021). So, we can get  $\frac{V_d^2}{d} \sim 5.349 \times 10^{-11}$  m s $^{-2}$ . As we will demonstrate below for M3, this is orders of magnitude lower than the acceleration caused by the cluster potential, thus it can be neglected.  $a_g$  is the acceleration due to the Galactic potential. Following Prager et al. (2017) it can be written,

$$a_g \cdot \vec{n} = -\cos(b) \left( \frac{\Theta_0^2}{R_0} \right) \left( \cos(l) + \frac{\beta}{\sin^2(l) + \beta^2} \right) \text{ m s}^{-2}, \quad (6)$$

where  $R_0$  is the distance of the Sun from the Galactic center ( $8.34 \pm 0.16$  kpc) and  $\Theta_0$  is the rotational speed of the Galaxy at the Sun's location ( $240 \pm 8$  km s $^{-1}$ ) (Sharma et al. 2014).  $\beta = (d/R_0)\cos(b) - \cos(l)$ , where  $l$  and  $b$  are the Galactic longitude and latitude of the GC, respectively. For M3,  $l = 42.22^\circ$  and  $b = 78.71^\circ$  giving  $a_g \sim -1.201 \times 10^{-12}$  m s $^{-2}$ . We notice that compared with the pulsar acceleration observed in M3 (for example,  $c(\frac{\dot{P}}{P})_{\text{obs}} \sim -5.478 \times 10^{-11}$  m s $^{-2}$  for PSR M3E), this effect is negligible, thus, we also ignore it.  $a_{\ell, \text{GC}}$  is the main contributive term (Freire et al. 2005) given by

$$a_{\ell, \text{GC}}(x) = \frac{9v^2}{d\theta_c} \frac{\ell}{x^3} \left( \frac{x}{\sqrt{1+x^2}} - \sinh^{-1}x \right), \quad (7)$$

where  $x$  is the distance from the pulsar to the center of the GC divided by its core radius ( $r_c = \theta_c d$ ),  $\theta_c$  is the core radius (0.37' for M3),  $v$  is the central stellar velocity dispersion, and  $\ell$  is the distance (also in core radii) to the plane of the sky that passes through the center of the GC. For the pulsars in M3, we can derive the upper limit of acceleration from  $\dot{P}_{\text{obs}}$  (assuming  $\dot{P}_{\text{int}} = 0$ ) (Lian et al. 2023)

$$a_{\ell, \text{P}, \text{max}} = c \left( \frac{\dot{P}}{P} \right)_{\text{obs}}, \quad (8)$$

In Figure 3, the blue dashed line represents the range of the maximum acceleration caused by cluster potential  $a_{\ell, \text{GC}}(x)$  along the radius of M3. The upper limit of acceleration for each pulsar from the observed spin period derivative is marked with a red triangle, and in the range of maximum acceleration of caused by the cluster potential. The spin period derivatives of PSRs M3A, E, and F were obtained. PSR M3A is close to the lower boundary of the range of the maximum acceleration due to the cluster potential. The real distance of M3A to the center can be larger than the projected angular separation. If so, it is possible that the real acceleration of M3A would be larger than the maximum.

### 3.5. The Scintillation

The scintillation bandwidth  $\Delta\nu_d$  and the scintillation timescale  $\Delta\tau_d$  can be used to quantify the average scintillation characteristics of each observation. Following Reardon et al. (2019), we obtained  $\Delta\tau_d$  by using a least-square fit to the one-dimensional time-domain ACF,

$$C(\Delta\tau, 0) = A \exp\left(-\left|\frac{\Delta\tau}{\Delta\tau_d}\right|^{\frac{5}{3}}\right), \quad (9)$$

and

$$C(0, 0) = A + W, \quad (10)$$

where  $A$  is constant to be fitted and  $W$  is the noise spike. After obtaining  $A$  and  $W$ , we fixed  $A$  and got  $\Delta\nu_d$  by doing a least-squares fit to the one-dimensional frequency-domain ACF via

$$C(0, \Delta\nu) = A \exp\left(-\left|\frac{\Delta\nu}{\Delta\nu_d/\ln 2}\right|\right), \quad (11)$$

Generally, the uncertainty of scintillation parameters comes from the uncertainty of the  $\chi^2$  fitting process and the statistical error caused by a finite number of scintles in the dynamic spectra (Bhat et al. 1999),

$$\sigma_r = \left( \frac{fBT}{\Delta\nu_d \Delta\tau_d} \right)^{-0.5}, \quad (12)$$

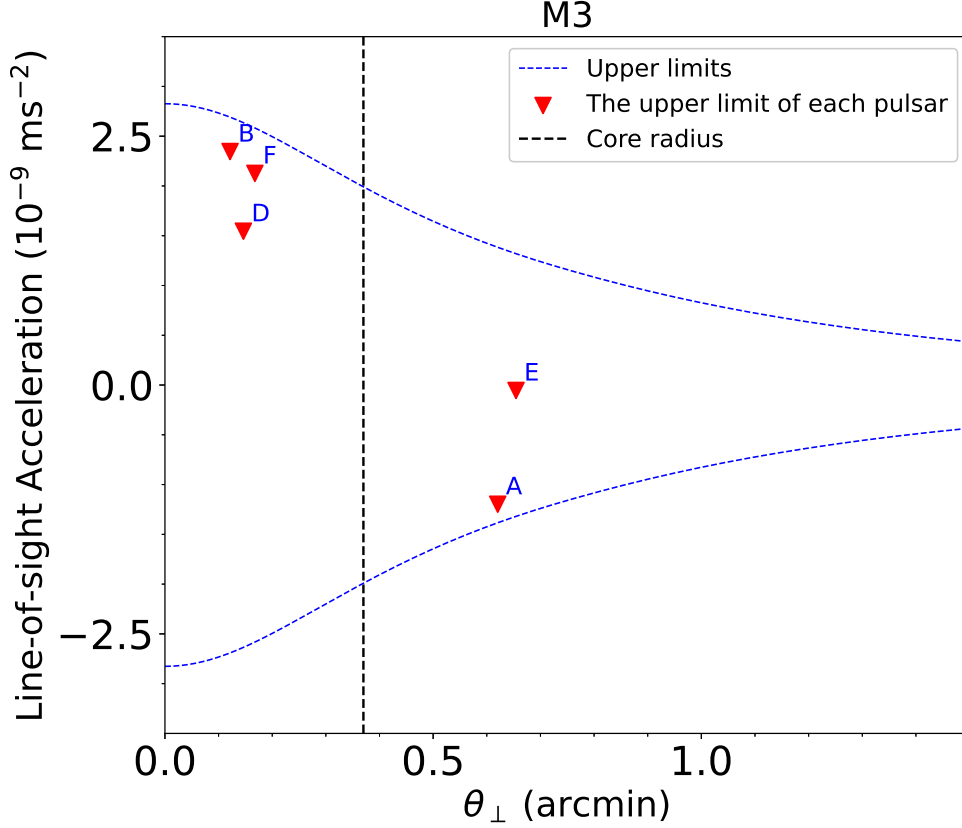


**Figure 3.** Acceleration model for M3. The blue dashed line represents the upper limits for the line-of-sight pulsar acceleration caused by cluster potential ( $a_{\ell,GC}$ ). The abscissa is the constant angular offset from the center ( $\theta_{\perp}$ ). The upper limit of acceleration for each pulsar from the observed spin period derivative was marked with the red triangle. The vertical dashed line represents the core radius ( $0.37'$ ).

where  $T$  and  $B$  are the integration time and bandwidth, respectively. The filling factor  $f$  is the percentage of scintillation area in the dynamic spectrum. We calculated the percentage of data with more than  $1\sigma$  in the dynamic spectra and chose  $f = 0.25$  in this work.

From [Rickett & Lyne \(1990\)](#); [Bhat et al. \(1999\)](#), the scintillation strength is

$$u \approx \sqrt{\frac{2\nu}{\Delta\nu_d}}, \quad (13)$$

where  $\nu$  is the central frequency (1250 MHz). When  $u < 1$ , it indicates weak scintillation. When  $u > 1$ , it indicates strong scintillation.

In some situations, we can detect arcs in the secondary spectrum. Scintillation arc can be described as [Reardon et al. \(2019\)](#)

$$f_{\lambda} = \eta f_t^2, \quad (14)$$

in which

$$\eta = 1.543 \times 10^7 \frac{D_{\text{kpc}} s (1-s)}{(V_{\text{eff},\perp} \cos \psi)^2}, \quad (15)$$

where  $\eta$  is the so-called arc curvature,  $D_{\text{kpc}}$  is pulsar distance in kpc,  $s$  is the relative distance of the scattering screen to the pulsar,  $\psi$  is the angle between the major axis of the anisotropic structure and the effective velocity vector, and  $V_{\text{eff},\perp}$  is the effective perpendicular velocity in  $\text{km s}^{-1}$ .

In Figure 4, we show the dynamic spectra, ACFs and the secondary spectra for PSRs M3A and B. We did ACF analysis for all M3 pulsars, and only obtained the scintillation parameters for PSRs M3A and B as shown in Table 4. We remind the reader that as only few patches are captured in most of the dynamic spectra, this may cause additional errors in the measurement of scintillation parameters.

**Table 4.** The scintillation parameters for PSRs M3A and B centered at 1250 MHz.

Pulsar Name	MJD	$A$	$W$	$\Delta\tau_d$ (min)	$\Delta\nu_d$ (MHz)	$\sigma_r$	$u$
M3A	58831	0.778±0.013	0.222±0.013	46.99±0.99	57.14±1.11	0.33	7
M3B	58831	0.821±0.006	0.179±0.006	60.02±0.55	52.99±0.49	0.36	7
M3B	59250	0.989±0.002	0.011±0.002	55.91±2.74	31.84±0.46	0.29	9
M3B	59524	0.973±0.008	0.027±0.008	34.43±2.24	39.58±0.80	0.29	8
M3B	59734	0.958±0.042	0.042±0.025	6.97±0.26	4.55 ±0.15	0.08	23

**Note.**  $A$  is constant to be fitted in equation 9 and  $W$  is the noise spike.  $\Delta\tau_d$  and  $\Delta\nu_d$  are the scintillation timescale and bandwidth, respectively.  $\sigma_r$  is the uncertainty.  $u$  is the scintillation strength.

In the secondary spectra, we only detected a clear scintillation arc for PSR M3B. Following Reardon et al. (2019), the arc curvature is  $649\pm 23 \text{ m}^{-1} \text{ mHz}^{-2}$ . It was noticed that there appears to be the beginnings of an arc in the secondary spectrum of PSR M3A, however because of the weakness of this signal it might be due to noise fluctuations and will not be discussed here.

For PSRs M3A and B, we did ACF analysis of the dynamic spectra at the same epoch (MJD 58831), and noticed that their scintillation bandwidths are basically the same. With such result, the scattering of PSRs M3A and B may be dominated by the same screen. More FAST simultaneous observations are needed to confirm this. For PSR M3B, we also analyzed ACF of the dynamic spectra at three other epochs (MJDs 59250, 59524 and 59734). From Table 4, we found that at the same epoch the scintillation timescale of PSRs M3A and B is different, and the scintillation timescale of PSR M3B is decreasing by approximately 53 min from MJD 58831 to 59734. We suggest that the differences in the scintillation timescales of PSRs M3A and B at the same epoch, as well as the variations in the scintillation timescales of PSR M3B with epoch, could be caused by combinations of the following reasons. Firstly, when fewer patches are captured in the dynamic spectra, this results in larger errors in the measurement of the scintillation timescale. Second, as PSRs M3A and B are in binary systems, even at same epoch PSRs M3A and B possess different orbital velocities and at different epochs the orbital velocity of PSR M3B varies with orbital phase. Third, for PSR M3B, compared with MJDs 58831, 59250 and 59524, the dynamic spectrum at MJD 59734 has more narrower patches and the scattering may come from different screen. In all the dynamic spectra of PSRs M3A and B, the scintillation strength  $u$  were 7, 7, 9, 8 and 23, respectively, indicating strong scintillation.

The tilted or asymmetrical patterns in the ACF diagrams of PSRs M3A and B indicate that the corresponding scattering medium is anisotropic. As described in Section 3.1, PSR M3A and B are all in binary systems. To date, as there no systematic drift velocity or orbital velocity measurements for M3 pulsars via VLBI (Very-long-baseline interferometry) or timing, we could not get the pulsar-to-screen distance from both the measured scintillation timescale and arc curvature by using Equation 15. For pulsars in binary system, multiple observations made at different orbital phases can help us to constrain orbital parameters through the study of the variations of scintillation timescale and arc curvature along orbital phases (Reardon et al. 2019). With more FAST observations in the future, our next work will be finding the location of the scattering screens and to constrain the orbital parameters for PSRs M3A and B.

#### 4. SUMMARY

The conclusions are as follows:

1. The timing solutions of previously known PSRs M3A, B, D, E, and F were either updated or obtained for the first time. With a timing baseline of 937 days, the spin frequency derivative, and the more accurate position of PSR M3A was measured. The timing solutions of PSRs M3B and D are consistent with previous results and updated. PSRs M3E and F are binaries with low mass companions. PSR M3E is in a 7.1-day orbit and with an eccentricity about  $1\times 10^{-4}$ . The orbital period of the PSR M3F circular orbit is about 3 days.

2. After searching 41 different observations with acceleration searches, the PSR M3C is still missing.

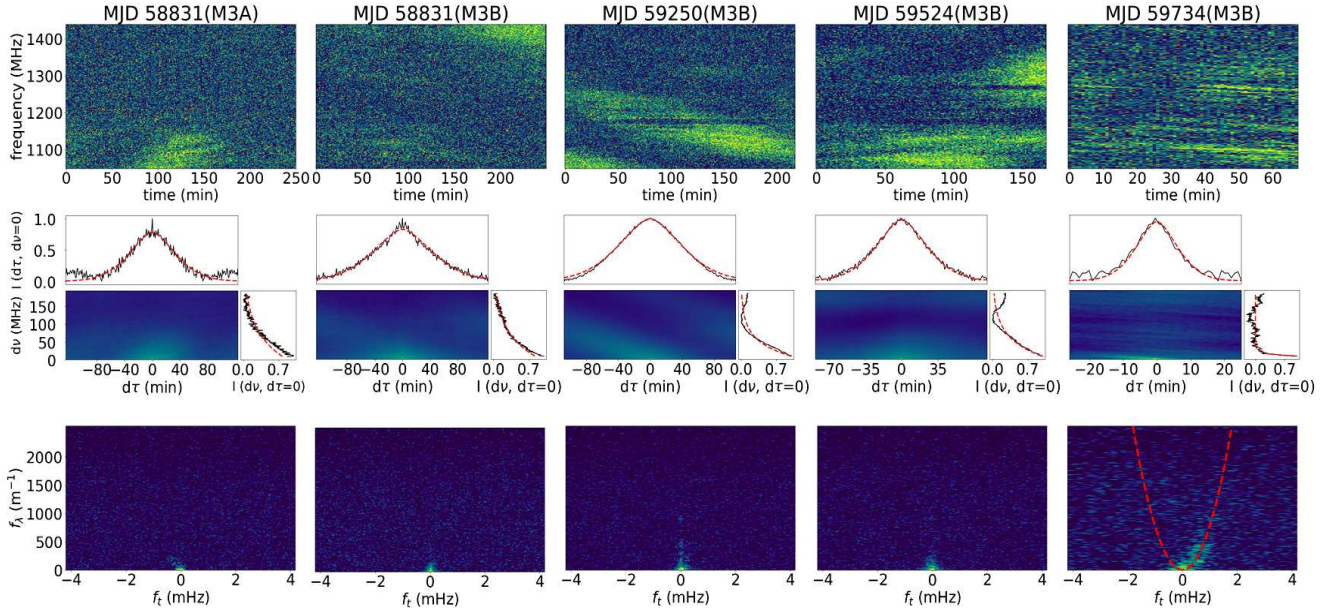


**Figure 4.** Dynamic spectra (top panels), ACFs (middle panels), and secondary spectra (bottom panels) of PSRs M3A and B. For PSRs M3A and B, the observations made on MJD 58831, 59250, 59524, 59734 are chosen to show in this figure. The data with more RFI in the first 1200 s are removed. The data duration of PSRs M3A and B are 249, 249, 216, 167, and 69 min, respectively. In these one-dimensional time-domain and frequency-domain ACFs, the red lines show the best-fit results for  $\Delta\tau_d$  and  $\Delta\nu_d$ , respectively. In all secondary spectra, in order to clearly identify the scintillation arcs, we cut the abscissa around  $\pm 4$  mHz. In secondary spectrum of PSR M3B, the red dotted line represent the best-fit arc curvature.

3. Due to the sensitivity of FAST, the detection rates of pulsars are several to ten times higher than those in [Hessels et al. \(2007\)](#), despite the very strong diffractive scintillation seen towards the cluster at these radio frequencies. Based on the searching results, the detection rates of PSRs M3A, B, D, E, and F are 58%, 90%, 78%, 51%, and 80%, respectively.

4. As predicted by the low single-binary encounter rate, the characteristics of pulsars in M3 seem to be similar to those of millisecond pulsars in Galactic disk.

5. From the dynamic spectra of PSRs M3A, B, and with the ACF analysis, the scintillation timescale ranges from  $7.0 \pm 0.3$  min to  $60.0 \pm 0.6$  min, and the scintillation bandwidth ranges from  $4.6 \pm 0.2$  MHz to  $57.1 \pm 1.1$  MHz. Based on the same epoch analysis, the scattering of PSRs M3A and B may be dominated by the same screen. The ISM which is dominating the scattering of PSRs M3A, and B is anisotropic. All the dynamic spectra of PSRs M3A, and B suggested strong scintillation. From the secondary spectra, only one scintillation arc of PSR M3B was obtained with a curvature of  $649 \pm 23 \text{ m}^{-1} \text{ mHz}^{-2}$ . Our next work will be on the scattering screens and the variation of scintillation parameters at different orbital phases.

This work is supported by the National Key R&D Program of China, No. 2022YFC2205202, No. 2020SKA0120100, the International Centre of Supernovae, Yunnan Key Laboratory (No. 202302AN360001 and 202302AN36000104), the National Natural Science Foundation of China under Grand No. 11703047, 11773041, U2031119, 12173052, 12173053, 12373032, 11963002, 12041304 and 12288102. Ju-Mei Yao was supported by the National Science Foundation of Xinjiang Uygur Autonomous Region (2022D01D85), the Major Science and Technology Program of Xinjiang Uygur Autonomous Region (2022A03013-2), the Tianchi Talent project, and the CAS Project for Young Scientists in Basic Research (YSBR-063), and the Tianshan talents program (2023TSYCTD0013). ZP and LQ are supported by the CAS “Light of West China” Program. ZP and LQ are supported by the Youth Innovation Promotion Association of the Chinese Academy of Sciences (ID nos. 2023064 and 2018075, Y2022027). RPE is supported by the Chinese Academy of Sciences President’s International Fellowship Initiative, Grant No. 2021FSM0004. This work is also supported by the International Centre of Supernovae, Yunnan Key Laboratory. This work made use of the data from FAST

(Five-hundred-meter Aperture Spherical radio Telescope). FAST is a Chinese national mega-science facility, operated by National Astronomical Observatories, Chinese Academy of Sciences.

## REFERENCES

- Balakrishnan, V., Freire, P. C. C., Ransom, S. M., et al. 2023, *ApJL*, 942, L35, doi: [10.3847/2041-8213/acae99](https://doi.org/10.3847/2041-8213/acae99)
- Bhat, N. D. R., Rao, A. P., & Gupta, Y. 1999, *ApJS*, 121, 483, doi: [10.1086/313198](https://doi.org/10.1086/313198)
- Blandford, R., Narayan, R., & Romani, R. W. 1986, *ApJL*, 301, L53, doi: [10.1086/184622](https://doi.org/10.1086/184622)
- Bogdanov, S., Bahramian, A., Heinke, C. O., et al. 2021, *ApJ*, 912, 124, doi: [10.3847/1538-4357/abee78](https://doi.org/10.3847/1538-4357/abee78)
- Cordes, J. M. 1986, *ApJ*, 311, 183, doi: [10.1086/164764](https://doi.org/10.1086/164764)
- Cordes, J. M., Pidwerbetsky, A., & Lovelace, R. V. E. 1986, *ApJ*, 310, 737, doi: [10.1086/164728](https://doi.org/10.1086/164728)
- Freire, P. C. C., Hessels, J. W. T., Nice, D. J., et al. 2005, *ApJ*, 621, 959, doi: [10.1086/427748](https://doi.org/10.1086/427748)
- Freire, P. C. C., Ridolfi, A., Kramer, M., et al. 2017, *MNRAS*, 471, 857, doi: [10.1093/mnras/stx1533](https://doi.org/10.1093/mnras/stx1533)
- Hamrick, P., Bansal, A., & Tock, K. 2021, *jaavso*, 49, 192
- Harris, W. E. 1996, *AJ*, 112, 1487, doi: [10.1086/118116](https://doi.org/10.1086/118116)
- Hessels, J. W. T., Ransom, S. M., Stairs, I. H., Kaspi, V. M., & Freire, P. C. C. 2007, *ApJ*, 670, 363, doi: [10.1086/521780](https://doi.org/10.1086/521780)
- Hill, A. S., Stinebring, D. R., Asplund, C. T., et al. 2005, *ApJL*, 619, L171, doi: [10.1086/428347](https://doi.org/10.1086/428347)
- Hotan, A. W., van Straten, W., & Manchester, R. N. 2004, *PASA*, 21, 302, doi: [10.1071/AS04022](https://doi.org/10.1071/AS04022)
- Hut, P., McMillan, S., Goodman, J., et al. 1992, *PASP*, 104, 981, doi: [10.1086/133085](https://doi.org/10.1086/133085)
- Jiang, P., Tang, N.-Y., Hou, L.-G., et al. 2020, *Research in Astronomy and Astrophysics*, 20, 064, doi: [10.1088/1674-4527/20/5/64](https://doi.org/10.1088/1674-4527/20/5/64)
- Lian, Y., Pan, Z., Zhang, H., et al. 2023, *ApJL*, 951, L37, doi: [10.3847/2041-8213/acdee7](https://doi.org/10.3847/2041-8213/acdee7)
- Libralato, M., Bellini, A., Vesperini, E., et al. 2022, *ApJ*, 934, 150, doi: [10.3847/1538-4357/ac7727](https://doi.org/10.3847/1538-4357/ac7727)
- Nan, R., Li, D., Jin, C., et al. 2011, *International Journal of Modern Physics D*, 20, 989, doi: [10.1142/S0218271811019335](https://doi.org/10.1142/S0218271811019335)
- Pan, Z., Qian, L., Ma, X., et al. 2021, *ApJL*, 915, L28, doi: [10.3847/2041-8213/ac0bbd](https://doi.org/10.3847/2041-8213/ac0bbd)
- Phinney, E. S. 1993, in *Astronomical Society of the Pacific Conference Series*, Vol. 50, *Structure and Dynamics of Globular Clusters*, ed. S. G. Djorgovski & G. Meylan, 141
- Prager, B. J., Ransom, S. M., Freire, P. C. C., et al. 2017, *ApJ*, 845, 148, doi: [10.3847/1538-4357/aa7ed7](https://doi.org/10.3847/1538-4357/aa7ed7)
- Ransom, S. 2011, *PRESTO: Pulsar Exploration and Search TOolkit*, *Astrophysics Source Code Library*, record ascl:1107.017
- Ransom, S., Hessels, J., Stairs, I., et al. 2005, in *Astronomical Society of the Pacific Conference Series*, Vol. 328, *Binary Radio Pulsars*, ed. F. A. Rasio & I. H. Stairs, 199
- Ransom, S. M. 2001, PhD thesis, Harvard University, Massachusetts
- Ransom, S. M., Stairs, I. H., Backer, D. C., et al. 2004, *ApJ*, 604, 328, doi: [10.1086/381730](https://doi.org/10.1086/381730)
- Rasio, F. A., & Heggie, D. C. 1995, *ApJL*, 445, L133, doi: [10.1086/187907](https://doi.org/10.1086/187907)
- Reardon, D. J. 2020, *Scintools: Pulsar scintillation data tools*, *Astrophysics Source Code Library*, record ascl:2011.019. <http://ascl.net/2011.019>
- Reardon, D. J., Coles, W. A., Hobbs, G., et al. 2019, *MNRAS*, 485, 4389, doi: [10.1093/mnras/stz643](https://doi.org/10.1093/mnras/stz643)
- Rickett, B. J. 1969, *Nature*, 221, 158, doi: [10.1038/221158a0](https://doi.org/10.1038/221158a0)
- . 1990, *ARA&A*, 28, 561, doi: [10.1146/annurev.aa.28.090190.003021](https://doi.org/10.1146/annurev.aa.28.090190.003021)
- Rickett, B. J., Coles, W. A., & Bourgois, G. 1984, *A&A*, 134, 390
- Rickett, B. J., & Lyne, A. G. 1990, *MNRAS*, 244, 68
- Sharma, S., Bland-Hawthorn, J., Binney, J., et al. 2014, *ApJ*, 793, 51, doi: [10.1088/0004-637X/793/1/51](https://doi.org/10.1088/0004-637X/793/1/51)
- Shklovskii, I. S. 1970, *Soviet Ast.*, 13, 562
- Sigurdsson, S., & Phinney, E. S. 1993, *ApJ*, 415, 631, doi: [10.1086/173190](https://doi.org/10.1086/173190)
- Stinebring, D. R., McLaughlin, M. A., Cordes, J. M., et al. 2001, *ApJL*, 549, L97, doi: [10.1086/319133](https://doi.org/10.1086/319133)
- van Straten, W., Demorest, P., & Osłowski, S. 2012, *Astronomical Research and Technology*, 9, 237, doi: [10.48550/arXiv.1205.6276](https://doi.org/10.48550/arXiv.1205.6276)
- Vasiliev, E., & Baumgardt, H. 2021, *MNRAS*, 505, 5978, doi: [10.1093/mnras/stab1475](https://doi.org/10.1093/mnras/stab1475)
- Verbunt, F., & Freire, P. C. C. 2014, *A&A*, 561, A11, doi: [10.1051/0004-6361/201321177](https://doi.org/10.1051/0004-6361/201321177)
- Wang, L., Peng, B., Stappers, B. W., et al. 2020, *ApJ*, 892, 43, doi: [10.3847/1538-4357/ab76cc](https://doi.org/10.3847/1538-4357/ab76cc)
- Wang, N., Manchester, R. N., Johnston, S., et al. 2005, *MNRAS*, 358, 270, doi: [10.1111/j.1365-2966.2005.08798.x](https://doi.org/10.1111/j.1365-2966.2005.08798.x)
- Wang, N., Yan, Z., Manchester, R. N., & Wang, H. X. 2008, *MNRAS*, 385, 1393, doi: [10.1111/j.1365-2966.2008.12864.x](https://doi.org/10.1111/j.1365-2966.2008.12864.x)

Yao, J.-M., Zhu, W.-W., Wang, P., et al. 2020, *Research in Astronomy and Astrophysics*, 20, 076,  
doi: [10.1088/1674-4527/20/5/76](https://doi.org/10.1088/1674-4527/20/5/76)

Yin, D.-J., Zhang, L.-Y., Li, B.-D., et al. 2023, *Research in Astronomy and Astrophysics*, 23, 055012,  
doi: [10.1088/1674-4527/acc37e](https://doi.org/10.1088/1674-4527/acc37e)

Zhang, D., Tao, Z., Yuan, M., et al. 2023, *Science China Physics, Mechanics, and Astronomy*, 66, 299511,  
doi: [10.1007/s11433-023-2138-5](https://doi.org/10.1007/s11433-023-2138-5)

Zhao, Y., Heinke, C. O., Cohn, H. N., Lugger, P. M., &  
Cool, A. M. 2019, *MNRAS*, 483, 4560,  
doi: [10.1093/mnras/sty3384](https://doi.org/10.1093/mnras/sty3384)